



LAWRENCE
LIVERMORE
NATIONAL
LABORATORY

Final Report for the San Jose State University Effort for Lawrence Livermore National Laboratory

M. S. Johnson, K. Parvin

January 17, 2013

Disclaimer

This document was prepared as an account of work sponsored by an agency of the United States government. Neither the United States government nor Lawrence Livermore National Security, LLC, nor any of their employees makes any warranty, expressed or implied, or assumes any legal liability or responsibility for the accuracy, completeness, or usefulness of any information, apparatus, product, or process disclosed, or represents that its use would not infringe privately owned rights. Reference herein to any specific commercial product, process, or service by trade name, trademark, manufacturer, or otherwise does not necessarily constitute or imply its endorsement, recommendation, or favoring by the United States government or Lawrence Livermore National Security, LLC. The views and opinions of authors expressed herein do not necessarily state or reflect those of the United States government or Lawrence Livermore National Security, LLC, and shall not be used for advertising or product endorsement purposes.

This work performed under the auspices of the U.S. Department of Energy by Lawrence Livermore National Laboratory under Contract DE-AC52-07NA27344.

Final Report for the San Jose State University Effort for Lawrence Livermore National Laboratory

Analysis of photonuclear reaction data.

K. Parvin¹ (PI), M. S. Johnson^{1,2} (Co-PI), R. Espinoza¹, M. Fong¹, T. Slauter¹.

¹*San Jose State University, San Jose CA 95192*

²*Lawrence Livermore National Laboratory, Livermore, CA 94550*

Executive Summary

This report is the conclusion of an effort of the Department of Physics and Astronomy at San Jose State University (SJSU) for Lawrence Livermore National Laboratory (LLNL). SJSU was tasked to assist with data analysis of recent photonuclear measurement data taken at Duke University's Free Electron Laser Laboratory (FELL) using the High Intensity Gamma-ray Source (HIGS). Specifically, photofission measurements of ²³⁵U near the fission barrier were performed at HIGS and the analysis of key aspects of that data were performed by SJSU. The results indicate that photofission of ²³⁵U is isotropic in azimuthal angle but shows angular dependence in the polar or laboratory angle. The conclusion is reached that the angular distribution is caused by the polarization of the beam which is 100% linearly polarized. Preliminary results using a novel method to extract the fission *J*-states indicate the dominate fission channel is through *J*=9/2. Results also indicate *J*=7/2 is the only other contributor to photofission.

Outline

This report is the convolution of reports drafted by the active participants (i.e. students at SJSU). These reports are included in this overall report as attachments. The reports discuss and detail the analysis of the participants for their efforts, which include: 1.) analysis of neutron detector data taken from online measurements (T. Slauter), 2.) analysis of flux measurement data taken offline (M. Fong), and 3.) overall results of photofission and width determination (R. Espinoza). The latter effort has transitioned into a thesis (M.S.) effort for Mr. Espinoza and the reporting here on his component is preliminary. We welcome future readers to contact SJSU for a copy of Mr. Espinoza's thesis when it becomes available (~May 2013).

Appendix 1: Analysis of neutron data from ^{235}U photofission.
T. Slauter (written by M. Fong)

Introduction

At the High Intensity Gamma-ray Source (HIGS), a Laser-Compton Back-Scattering Photon Source (LCBS) at Duke University, a gamma-ray beam, is created by colliding electrons moving near the speed of light with a laser (produced with a Free Electron Laser) with energy $\sim \text{eV}$ aimed antiparallel to the electrons momentum. When the incident laser photons interact with the electron bunch the photons up-scatters in energy ranging from keV to MeV, a gamma-ray The gamma-ray beams are short pulses (with a period of 179 ns) of light that are produced as either circular or linear polarizations.

When a gamma-ray photon is absorbed by a nucleus the nucleus gains energy approximately equal to the incident photon energy. The nucleus will undergo fission if the excitation energy is at or near the fission barrier, where it will break apart into daughter products. This process is called photofission. The purpose of this experiment is to measure the prompt neutrons and determine their angular distributions and azimuthal asymmetries from photofission in ^{235}U .

The fission target is surrounded by an array of 18 detectors 57 cm equidistant from the target. These detectors count the neutrons that are produced from photofission by reading the amount of neutrons hitting the array. The gamma-ray beam pulsed is providing a short window for the photofission process. Energy of the neutron is found from the time of flight technique. The time difference between the pulse and the neutron hit is be easily converted to neutron speed $v = \frac{\Delta x}{\Delta t}$ where $\Delta x = 57\text{cm}$. The calculated

speed of the neutrons gives us $E = \frac{1}{2}mv^2$; m= mass of the neutron and v = speed of the neutron. Notice we have assumed non-relativistic momentum.

Twelve of the 18 detectors surrounding the target are placed at $\theta = 55^\circ, 90^\circ, \text{ and } 125^\circ$ and at $\varphi = 0^\circ, 90^\circ, 180^\circ, \text{ and } 270^\circ$; six detectors were placed at $\theta = 72^\circ, 107^\circ, \text{ and } 142^\circ$ and at $\varphi = 0^\circ \text{ and } 90^\circ$. The detector hit gives us the angle at which that specific neutron broke up from the nucleus. The energy and the angle of separation (angle in between the momentum of the incident gamma-ray beam and the fission neutron's momentum) give us the data we seek. For more experimental details see thesis work by Ruben Espinoza (May 2013)

When a nucleus absorbs energy from the photon, it could disperse that energy in many ways through the fission channel. The nucleus could fission into many fragments—combinations of protons and neutrons. One fragment carries a varying fraction of the total energy that the nucleus had before fission, where another fragment might carry another energy different from the difference of the absorbed energy and the kinetic energy of the other daughter. These fragments fly outward from the original nucleus and undergo neutron evaporation. The story becomes much more complicated as the momentum distribution of the neutrons are convolutions of a very random statistical set of processes.

Given the complexity of the resultant neutron energy from the fission process the neutron energy measured is a continuum and is empirically modeled and is called the Watt Spectrum. The Watt spectrum is given by W and the free-parameters are a and b. The free-parameters are determined through a fitting procedure. The Watt Spectrum is expressed by

$$W(a, b, E') = C e^{-aE'} \sinh [(bE')^{\frac{1}{2}}]$$

Eq. 1: Analytical function Watt Spectrum. [1]

$W(a, b, E')$, where $C = \left(\frac{\pi b}{4a}\right)^{\frac{1}{2}} \frac{e^{\left(\frac{b}{4a}\right)}}{a}$. E' is the secondary energy (energy of the fission neutrons) and coefficients a and b depend on the isotope and vary weakly with incident neutron energy (details taken from [1]).

Since the neutron dissociation channel is open, we must discriminate between dissociated neutron and fission neutrons. The incident energies for these measurements were near the separation threshold such that the dissociated neutrons were at or below ~ 1 MeV. Therefore, we could discriminate fission neutrons by fitting the neutron spectral region above 1 MeV. From the fitting procedure we could extract the fit parameters and determine the neutron count rate in each detector.

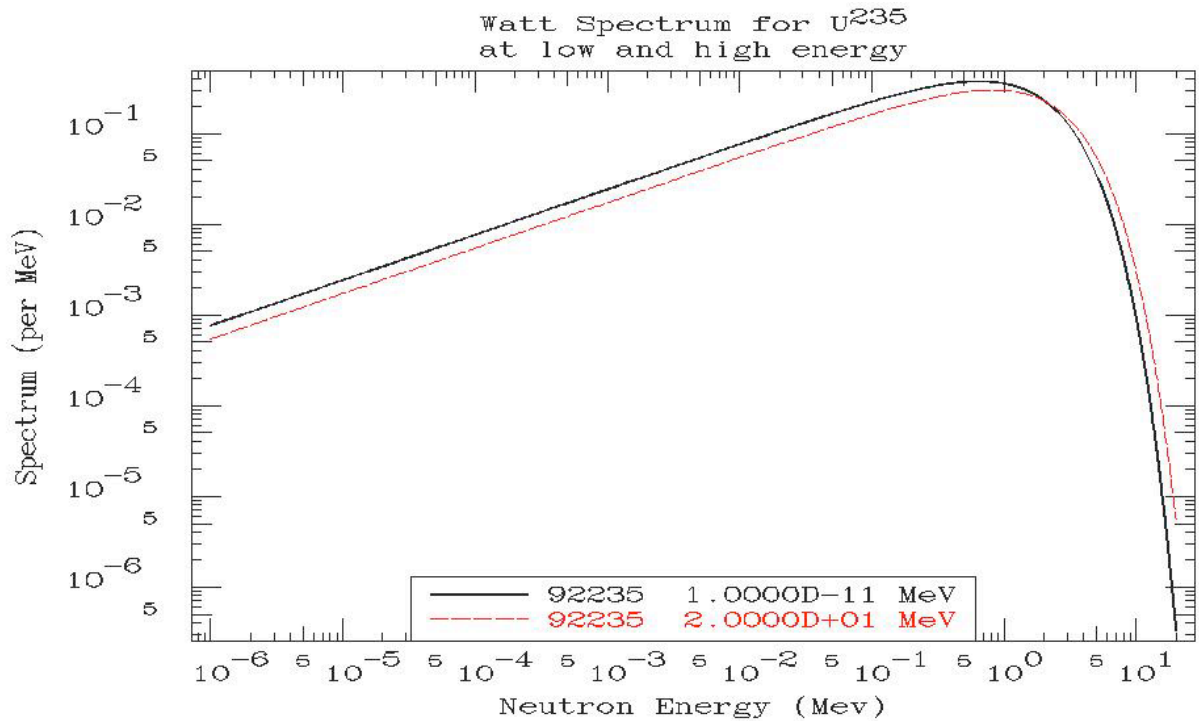


Fig. 1: Watt spectrum for Uranium 235 at low and high energies. Figure taken from [1]

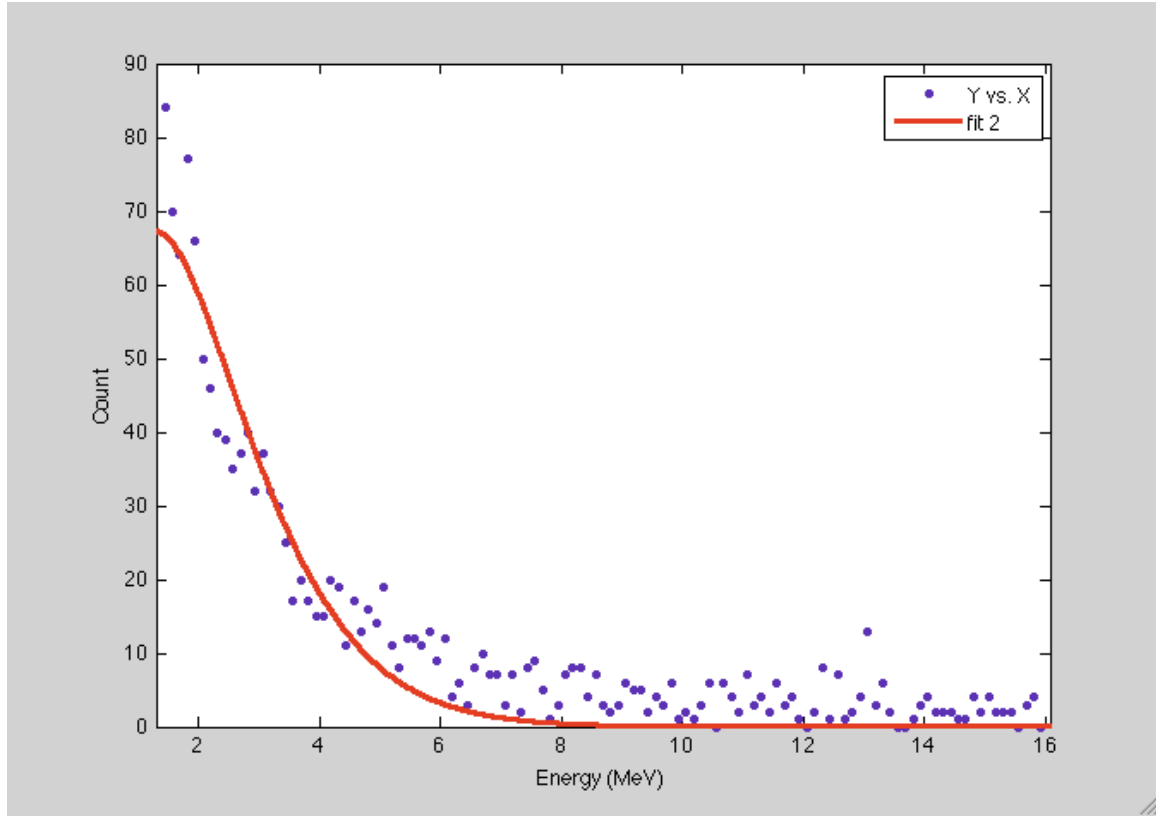


Fig. 2: Example (Run 14, Energy 4.976 MeV detector 4) with Chi-Squared=2.9281.

Fig. 2 shows the hits on a detector four as a function of energy, where $E > 1\text{ MeV}$. The curve is a fit to the data using Eq.1. The variables for the Watt Spectrum equation are given from the fit. A χ^2 test is applied to the fit and the variance of the free variables are recorded.

The angular distribution is extracted from an integral array, where the values are taken with respect to the detector location.

The variance in the free variables are

$$Var(a) = \left(\frac{aa - a}{2}\right)^2$$

Eq. 2: Variance in free parameter "a."

An Integral of Degrees of Freedom (*IntDof*) in the free parameters is taken by using the trapezoidal method with unit spacing. The combination of the variance and integral of the degrees of freedom can determine the Integral Variance:

$$Integral\ Variance = Var(a) * IntDof(a)^2 + Var(b) * IntDof(b)^2$$

Eq. 3: Integral variance. "a" and "b" are the free parameters.

The Integral Standard Deviation is the square root of the integral variance.

Appendix 2: Analysis of HIGS flux data

M. Fong

Photon Energy Analysis

Introduction

Laser-Compton Back-Scattering Photon Sources (LCBS) are important tools for photonuclear physics. Photonuclear physics studies nuclear structure and nuclear reactions with photons. These processes are studied and applied in a variety of fields such as astrophysics, nuclear reactors, etc... The typical LCBS energies are about an MeV and higher. These energies are important for nuclear physics.

The spectral details of the LCBS must be known with high precision and accuracy in order to study photonuclear processes. We present the analysis and techniques of measuring the spectral features of the LCBS at Duke University, known as the High Intensity Gamma-ray Source (HIGS). The analysis of the HIGS beam is crucial for experiments and is performed here.

A LCBS provides is partly an accelerator used to accelerate the speed of electrons to near the speed of light. A laser with energy $\sim eV$ is aimed at a chosen angle to the electrons momentum. The incident laser interacts with the electron bunch, backscatters and produces photons with energy ranging from keV to MeV –depending on the electron and laser energies.

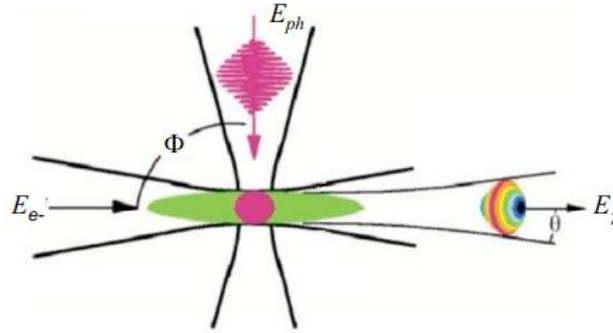


Fig. 1: Model of an electron colliding with a photon. Incident photon of energy E_{ph} is aimed at an electron at an angle Φ with energy E_{e-} , producing a gamma ray of energy E_γ . Figure taken from [1]

In the ideal case, the gamma spectrum from a LCBS would show a delta function according to Eq. 1, where we would assume uniform momentum of the electron bunch. In practice, the electrons are not moving with a unidirectional momentum because there are interactions within the electron bunch and other effects from the accelerator's electromagnetic optics. Therefore, we expect a spread of the produced photon energies (E_γ) are not all equal. Details of the spectral shape of the photon beam is critical for photonuclear measurements.

$$E_{\gamma} = \frac{E_{ph}(1 - \beta \cos \varphi)}{[(1 - \beta \cos \theta) + E_{ph}(1 - \cos(\theta - \varphi))/E_{e^-}]}$$

Eq. 1: Equation representing the model above. [1]

In the case of the HIGS facility $\varphi \cong \pi$, $\beta \cong 1$, $\theta \cong 0$, which is approximated by:

$$E_{\gamma} \cong \frac{E_{ph}(2)}{[E_{ph}(2)]/E_{e^-}} \cong E_{e^-}$$

Interactions with Matter

Photons interact with matter in a variety of ways, e.g. coherent or incoherent. Some of these interactions occur are photoelectric absorption, Compton scattering, pair production, triplet production, photodisintegration, etc... For the purposes of this paper, the reactions that are the most important are Photoelectric Effect, Compton Scattering, and Pair Production. The importance of the interactions will become more apparent later.

Photoelectric Effect:

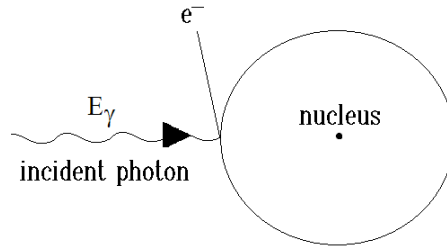


Fig. 2: Model of incident photon with orbiting electron. Incident photon energy E_{γ} is absorbed by an atom. With enough energy, the electron will escapes.

In a given material, there are electrons that orbit constituent atoms. The photoelectric effect occurs when an incident photon is absorbed by the atom, knocking an electron out, provided the photon has enough energy to overcome the work function energy (which is dependent on the atom). The liberated electron will leave a hole whereby another electron will drop from its shell to fill the hole. This situation produces a photoelectron and also an X-ray. The photoelectrons energy is $E = E_{\gamma} - \Phi$, where E is the energy of the liberated electron, E_{γ} is the energy of the incident photon, and Φ is with work function energy that is required for the electron to be expelled from the atom.

Compton Scattering:

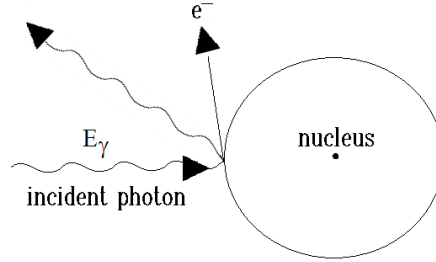


Fig. 3: Model of incident photon interacting with orbiting electron. The incident photon scatters with energy E' , while the electron escapes the atom with energy E .

Compton scattering occurs when an incident gamma-ray interacts with a free or bound electron. The photon is then scattered and the electron recoils, where the energy from the incident photon gives some energy to the free electron. The energy of the recoiled electron is $E = E_\gamma - E'$, where E_γ is the incident photon, and E' is the energy of the scattered photon. An alternative way of writing it is:

$$E = E_\gamma \frac{\frac{E_\gamma(1 - \cos\theta)}{mc^2}}{1 + \frac{E_\gamma(1 - \cos\theta)}{mc^2}}$$

Eq. 2: Energy of recoiled electron. Equation taken from [2]

m = rest mass of electron, θ = deflected angle. This shows that there are two extremes, where $\theta = 0$ or $\theta = \pi$. At $\theta = 0$ the scattered photon gives no energy to the electron. When $\theta = \pi$, the incident photon is backscattered and the electron moves in the direction of incidence; a maximum energy transfer between the photon and electron. The energy of the backscattered photon ($\theta = \pi$) is:

$$E' = \frac{E_\gamma}{1 + 2E_\gamma/mc^2}$$

Eq. 3: Energy of backscattered photon. Equation taken from [2]

Compton scattering also occurs for bound electrons with the same kinematics but the interaction cross-section is modified by atomic form factors which take into account the bound nature of the electron.

Pair Production:

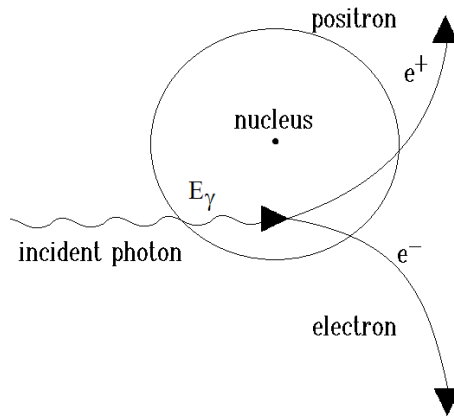


Fig. 4: Model of incident photon near nucleus, producing positron and electron. Incident photon interacts with a nucleus, gaining enough energy to create the pair; at least the total rest mass energy of the positron and electron.

If the photon has enough energy, the photon could turn into a electron-positron pair, where the photon would have to have at least energy equal to $2mc^2$. This occurs when the photon is near the nuclei of the constituent atoms, giving energies:

$$E_- + E_+ = E_\gamma - 2mc^2$$

Eq. 4: Equation for pair production.

E_- = energy of electron, E_+ = energy of positron.

Cross Section:

These interactions occur with a certain probability, or “cross section,” which may be energy dependent. The processes discussed above—Photoelectric absorption, Compton scattering, and pair production cross sections, depend on incident photon energy.

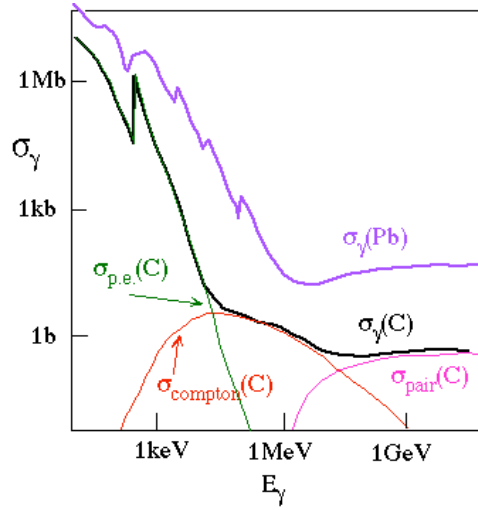


Fig. 5: Cross section with different elements; e.g. C (Carbon), Pb (Lead). Lead cross section is there for comparison (Larger Z). σ_γ is the total cross section. Figure taken from [3]

The total cross-section is the sum of partial cross-sections, e.g. σ_γ = total cross section, which for our discussion is made of: $\sigma_{p.e.}$ = photoelectric effect, $\sigma_{compton}$ = Compton scattering cross section, σ_{pair} = pair production cross sections (see Fig. 5 and Eq. 5). The cross section vs. energy plot (in Fig. 5) shows that with increasing energies, the more likely one interaction with matter will dominate over the others. For example, with energies $E_\gamma > 1\text{MeV}$, the plot shows that pair production grows to be the most dominant.

$$\sigma_\gamma(E_\gamma) = \sigma_{p.e.}(E_\gamma) + \sigma_{compton}(E_\gamma) + \sigma_{pair}(E_\gamma)$$

Eq. 5: Equation for the total cross section at a particular energy.

Detector Response

A detector measures energy of a particle by measuring its energy deposition. In some detectors energy deposition causes electrons to be liberated and the electrons are collected with an electric field onto an anode. Charge sensitive electronics attached to the anode collect, amplify, and shape a signal to be analyzed and recorded. For our measurements we use a High Purity Germanium (HPGe) detector that works according to this approach. As the incident photon interacts with the matter of the detector, interactions will occur. Ideally, when the interactions occur, energy is absorbed by the detector and is equal to that of the energy of the incident photon. However, in practice not all energy is deposited into the crystal due to escaping secondaries from the detector.

The HPGe Detector:

HPGe (High Purity Germanium) detectors take advantage of its semiconductor properties that allow for high resolution gamma-ray spectroscopy (Counts of discrete energy levels). The crystal lattice of the ultrapure germanium material sets up an energy gap (or band gap) between the valence and conduction bands, low enough for very sensitive energy readings. The electrons naturally are bound to the lower, valence band. With enough incident energy the electrons can absorb that energy and jump to the conduction band; where the electrons in this band are able to move freely throughout the crystal. The effected electron in that case has left a hole in the valence band. The combination of the two is an electron-hole pair. These moving electrons give us an opportunity to read the electrical conductivity of the germanium.

To obtain a high-resolution detector, small band gaps are important. Having small band gaps allow the detector to distinguish between small energy differences. Since the energy gap is small the detector is sensitive to temperature since electrons could gain energy from the environments heat. So using semiconductors with small band gaps, the material must be cooled in order for it to yield any useful readings; maintained at 77 K by using liquid nitrogen. As a result the HPGe detector has 2 keV resolution.

Escaping Events:

If no energy escapes, the record energy will be equal to the incident photon energy. Interactions near the edge of the detector sometimes result in escaping energies:

In the case of the photoelectric effect, when an electron absorbs energy from a photon, provided that it is enough energy to overcome the work function of the material, the electron is ejected. The hole left from the ejected electron is filled by another electron; producing an X-ray (or Auger electron) with energy equivalent to the energy lost by the electron dropping to a lower state. If the photoelectron has enough energy to overcome the electric field of the detector, it may escape the detector, thus the escaping electron's energy will not be recorded, producing a lower energy reading.

For Compton scattering, the energy of the recoiled electron or scattered photon depends on the angle of incidence. The range of $0 < \theta < \pi$ produces a continuum of energies that can be transferred to the electron. This is called the Compton continuum, where $\theta = \pi$ is the Compton edge. This continuum will show up in the spectrum. If this occurs near the edge of the detector and the energy escapes, it will produce a lower energy reading.

In pair production, when the photon interacts with the nucleus of an atom, the photon could produce a positron electron pair. If the positron annihilates with an electron, two 0.511 MeV photons will be produced. If one of these escapes the detector, it will leave a lower energy reading 0.511 MeV less than the incident photon. If two escape, it will result in 1.022 MeV less energy than the incident photon. Both will produce a lower energy reading (which we will later refer to as the single and double escape peaks).

When photoelectric effect, Compton scattering, and pair production would have energies escaping the detector, the detector would read a lower energy deposition than the incident photon energy. The escaping electrons and photons are due to these events occurring near the edge of the detector.

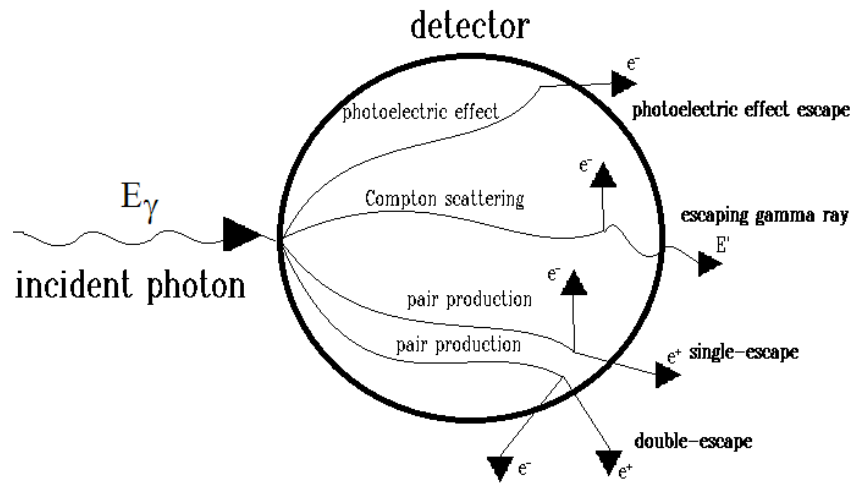


Fig. 5: Incident photon interactions with matter near the edges of the detector, showing escaping energies that result in lower energy deposition.

The full and partial energy depositions ubiquitous for all detector types, (c.f. Fig. 6).

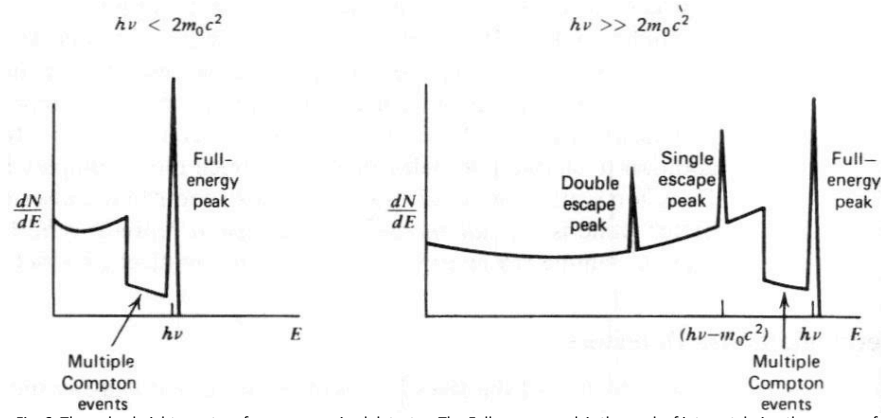


Fig. 6: The pulse-height spectra of an average-sized detector. The Full-energy peak is the peak of interest, being the energy of the incident photon beam. The single-escape peak is due to $m_0c^2 = 0.511 \text{ MeV}$ escaping photon. The double-escape peak is due to two escaping photons $2m_0c^2 = 1.022 \text{ MeV}$. Between the single-escape peak and the full-energy peak is the Compton edge, where preceding the edge is the Compton continuum. Figure taken from [2]

Analysis determines the incident energies would be the full-energy peak furthest to the right (see Fig. 6). In some cases for $E < 2mc^2$, the spectrum only contains a Compton continuum, since the only escape events possible in the energy range are Compton (left Fig. 6). For $E > 2mc^2$, the pair-production escape events become prominent and are seen in Fig. 6 (right).

However, in the spectra there are (generally) two other peaks to the left of it, which is due to the escaping electrons or gamma rays from the detector. The energies that leave the detector yields lower energy readings (or counts) than the incident photon beam of interest.

Analysis

The energies of the HIGS beam for these measurements are $\gg 2mc^2$, which allows for single and double escape events. The pair production cross section dwarfs the Compton effect cross section, where the Compton continuum is too small to see with respect to our energy scales.

Figure 6 shows the spectral shape of the HIGS beam with the HPGe response in comparison to an ideal HPGe detector.

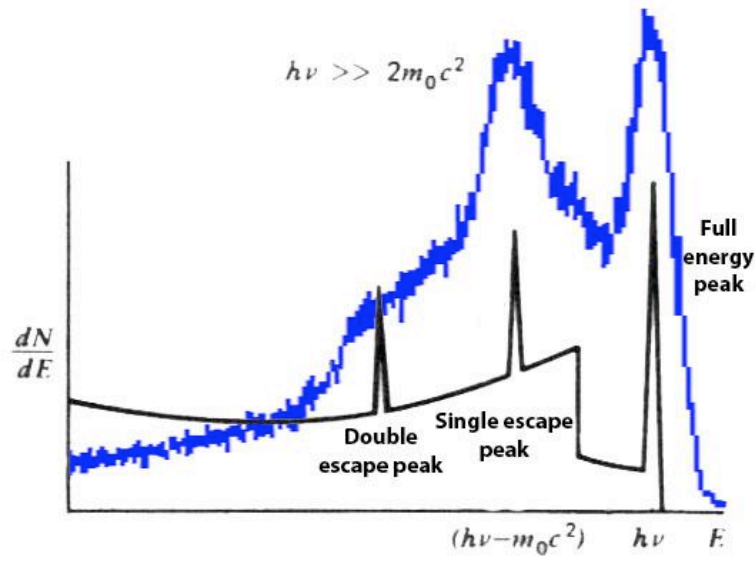


Fig. 7: The blue is a typical spectral shape of the HIGS beam with the HPGe response overlaid with an ideal HPGe detector pulse-height spectra. Overlaid with [2].

Due to the practicalities discussed previously, the produced beam from HIGS is not a delta function, but is a broad Gaussian curve. In Fig. 7 the double escape, single escape, and full energy peaks can easily be identified. A little more difficult to see perhaps, is the Compton edge in between the single escape and full energy peak. What should be a deeper valley in between the peaks is muddled with the Compton edge, the continuum preceding it, and also the overlap of the single escape peak and the full energy peak.

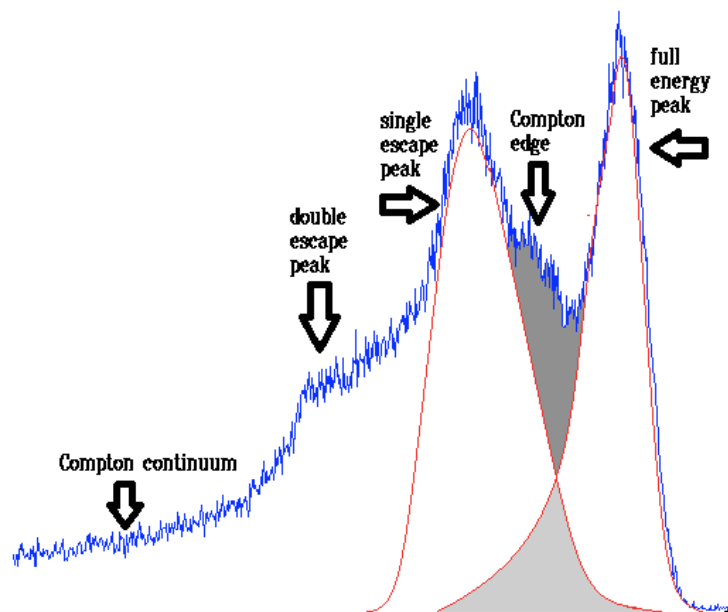


Fig. 8: Run2235 with "Gaussian fits" over the single escape and full energy peak. Overlap of the two Gaussians as well as the Compton continuum and edge contribute to the higher counts in energy in between the single escape and full energy peaks.

Fig. 8 shows the Compton continuum, Compton edge, single escape and full energy peak overlaps, contributing to the higher counts in energy between the two peaks in dark grey. Because there are overlaps between the single escape peak and the full-energy peak, this must be taken into consideration whilst analyzing the data.

The data:

The gamma spectrum contains background radiation known as Naturally Occurring Radioactive Material (NORM). NORM is present in the material of the detector, the equipment involved in the set up, terrestrial radiation, laboratory materials, far-away structures, environment (air) the detector is in, etc.... NORM includes radioactive decays from ^{232}Th , and ^{40}K .

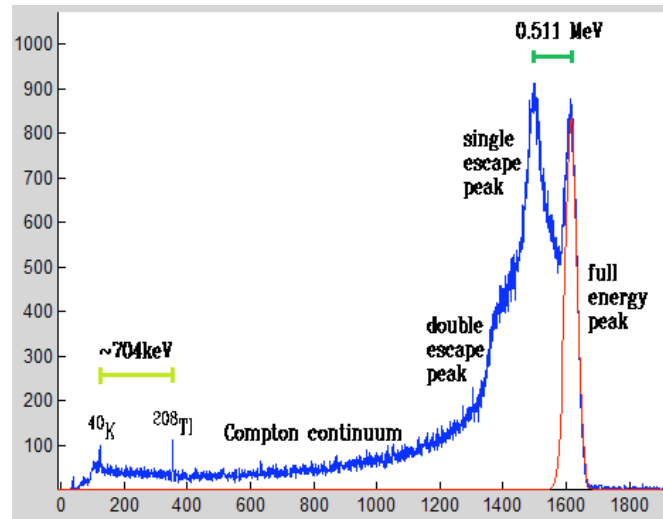


Fig. 9: A typical spectral shape of the HIGS beam with the HPGe response with a Gaussian fit over the full energy peak. On the left is background radiation due to ^{40}K and ^{208}Tl . (Run number 2255)

The HIGS beam with the HPGe response spectrum (Fig. 9) shows background radiation on the left with energies ~ 1461 keV for ^{40}K and ~ 2165 keV for ^{208}Tl . The NORM provides an online calibration source. That is to say, the difference between the two energies and their placements on the spectrum can be used to scale the bin numbers with energy. Using a linear analysis while $x = \text{bin number}$, $E = \text{energy}$, $m = \frac{\Delta E}{\Delta x}$: $E = mx + b$. Here $\Delta E = 704$ keV and $\Delta x = 230.3$, so $m = 3.05$ keV. Now the energies of the peaks can be determined with $E = (3.05 \text{ keV}) * x + b$.

Approximating the bin number of the full energy and single escape peaks, we have $x(\text{full energy peak}) = 1614$, $x(\text{single escape peak}) = 1499$, $\Delta x = 115$. We know that between the single escape and full energy peak $\Delta E = 511$ keV. $\Delta E = (3.05 \text{ keV})\Delta x + b$ shows that $b = 511 \text{ keV} - (3.05 \text{ keV}) * 115 = 161 \text{ keV}$. Using the values for m and b , and the equation $E =$

$(3.05 \text{ keV}) * x + (161 \text{ keV})$, we can easily determine the value of the peak energy in units that are useful for nuclear measurements.

As stated before, our interest is the full energy peak and its shape. In this experiment the most important energy to know is the incident energy; or centroid of the full energy peak. To obtain the centroid a Gaussian is fitted over the full energy peak (Fig. 10).

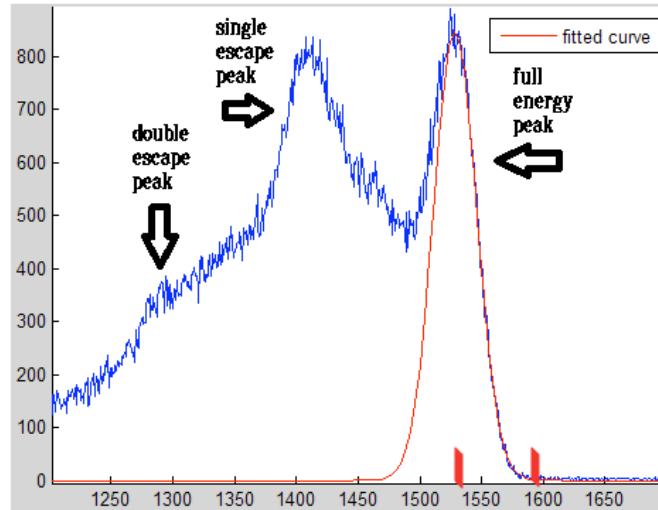


Fig. 10: Zoomed about the double escape, single escape, and full energy peaks. The two red marks are the lower and upper bound this Gaussian fit represents. (run 2304).

Fig. 10 is a typical example of the spectra produced from our HPGe detector. The peak of interest is the full energy peak; furthest to the right. The HIGS produces a Gaussian peak shape, which implies a Gaussian fit (red curve in Fig. 10).

To obtain the full energy peak (which allows us to get the energy) we must find the Gaussian that best represents it. In choosing the lower and upper bounds of the Gaussian fit, one must take into consideration the contribution of the Compton continuum, Compton edge, and single escape peak to the full energy peak. The lower bound is chosen near the top of the full energy peak apex to avoid the overlap. The upper bound is easy to choose—as long as it is chosen near the base of the peak (This will be discussed later).

The fit relies heavily on the low band channel. If the low band channel is too low, then the Gaussian would misestimate the contribution of the lower energy counts into the full peak. If the low

band channel is chosen after the apex of the full energy peak, that Gaussian would represent a different fit (with a much higher apex) than the data provided (Figure 11).

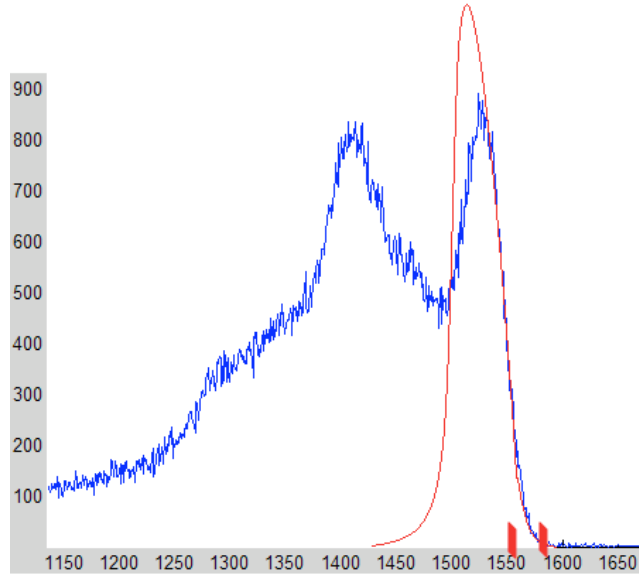


Fig. 11: Low bound chosen after the apex of the full-energy peak. "Gaussian fit" that does not represent the data.

Fig. 11 shows that if the high band channel is chosen too close to the peak, it will also result in a poor Gaussian fit. When the high band channel is chosen near the base of full-energy peak, the Gaussian varies little. This is because there are enough data points preceding the high band channel to contribute to a more accurate Gaussian fit.

When the lower and upper bound are chosen about the full energy peak, the specified spectra is fitted with the Gaussian:

$$f(x) = Ae^{-\left[\frac{x-\mu}{\sigma\sqrt{2}}\right]^2}$$

Eq. 6: The height, centroid, and width are given by A , μ , and σ respectively.

χ^2 test:

The Chi-squared (χ^2 ; Chi2) test is an important tool in data analysis. The Chi-squared test measures the precision of the fit to a model, in this case a Gaussian peak shape. Important parameters for this model are: height, centroid, and width of the Gaussian and the chosen boundaries.

The boundaries can be graded by way of the Chi-squared test, and we do that by varying the lower and upper bounds until the best fit is found. Using MATLAB, a script was written (Appendix) to make this prescription efficient, since there were many data sets to apply to. The approach is accomplished by keeping the lower bound constant while varying the upper bound, fitting and doing the χ^2 test with each attempt. Then it moves the lower bound up one channel and sweeps the same upper boundary range. The fit and χ^2 test is done, then repeats.

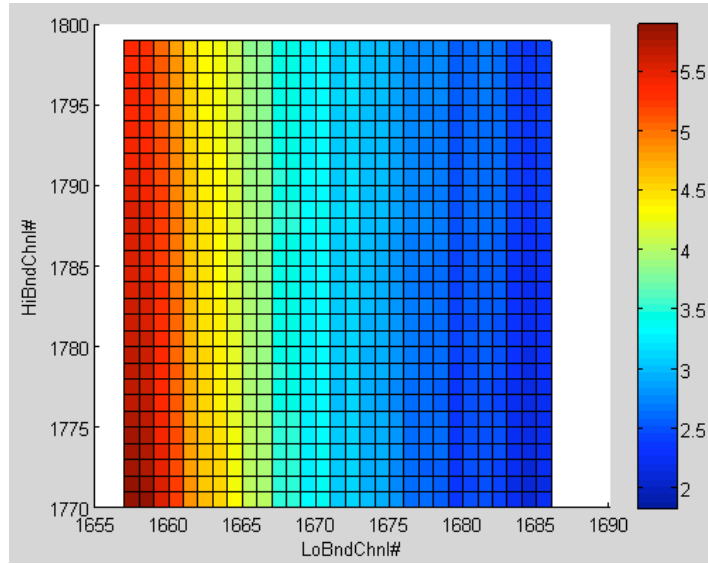


Fig. 12: LoBndChnl# is the lower bound channel numbers, HiBndChnl# is the high bound channel numbers, and the values of χ^2 are color coded with respect to the color spectrum on the right. (Run 2211)

The result is a χ^2 3D contour (Fig. 12) with dependencies on the lower and upper channel numbers. The upper limit for the low band channel (LoBndCnl#) is chosen at the apex of the full energy peak.

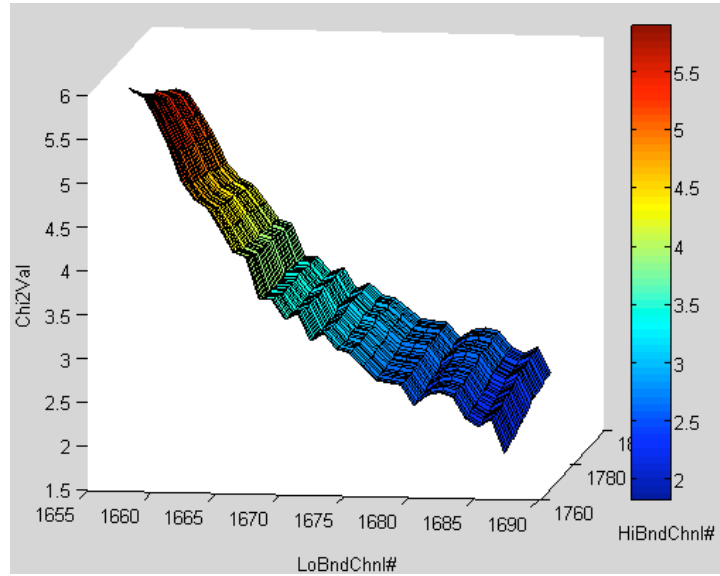


Fig. 13: This is a side view of the χ^2 3D contour. The high channel limits hardly varies the accuracy of the Gaussian fit; as most 3D χ^2 contours show. This is a Chi2 3D contour with only the useful data (extracted lower bound data points above the full-energy peak apex).

Clearly the results indicate that there is a strong dependence on the lower channel, but virtually none on the upper channel. This is expected because of the convolution of the other spectral features discussed previously. The upper channel is not as sensitive because the model (Gaussian) in this region is a good representation.

Results

Tab. 1 shows the important values representing the best fit for the corresponding run number. It's significant figures has also been reduced in order to fit the table and the (+/-) is the average of the upper and lower bound of the uncertainties. The complete table will be in the Apendix.

High channel	Low Value	High Value	Minimum Chi2 Value	A	A(+/-)	μ (keV)	μ (+/-)	σ (keV)	σ (+/-)
2000	1443.03	1511.4	3.4119575	2321.792	19.24759	4573.621	162.5591	217.0213	162.1038
1735	1211.08	1295.72	1.7148327	1056.078	19.43342	3846.094	163.1666	206.9697	162.1663
1749	1227.35	1307.11	2.2386795	890.2631	9.859992	3913.265	162.8102	209.8015	162.2642
1771	1255.84	1325.02	1.8278923	915.7201	17.32144	3991.617	163.9412	212.0618	162.811
1814	1277	1360.02	3.5207375	1902.083	15.80878	4064.54	162.4681	213.9831	162.0114

1807	5381.46	5593.25	1.3859168	700.874	11.53769	16599.94	172.5241	373.7767	168.7101
1810	5371.37	5603.34	0.5110598	61.77883	2.202179	16594.86	184.8691	364.2523	178.8802
1869	1303.86	1404.78	1.5421456	959.8349	10.34933	4142.007	162.7492	211.4041	162.1389
1892	1319.32	1423.5	2.3338503	897.7181	8.154014	4199.696	162.5836	213.4531	162.1866
1961	5563	6110.98	2.3829376	692.6268	6.196413	17171.14	167.5587	379.445	165.6263
1927	1364.9	1451.99	1.7918749	911.44	11.10232	4339.072	162.6454	212.7927	162.2199
2661	1395.02	2049.39	2.3370577	943.1725	4.380594	4423.79	161.8783	218.2279	161.5939
1943	1390.13	1465.01	1.0111984	175.7773	3.761086	4410.54	170.4084	222.4258	165.2637
1987	1425.13	1500.82	1.7670554	312.0255	6.753082	4515.983	164.7599	213.1639	163.5834
1982	1429.2	1496.75	3.3667477	939.0127	24.92703	4516.989	164.9913	213.1889	163.3468
2049	1464.2	1551.28	1.9611013	897.05	10.03602	4635.388	162.9621	213.6096	162.3511
2050	1474.78	1552.1	1.8216976	819.4194	11.34876	4667.062	163.3441	211.8509	162.6081
2065	1475.59	1564.31	2.9545709	955.6979	15.51105	4663.265	163.6278	213.1016	162.6486
2082	1497.57	1578.14	1.8803308	853.0467	9.192597	4739.094	162.9596	215.2066	162.3788
2101	1523.61	1593.61	2.1649903	836.2175	13.72908	4811.921	163.6718	211.7885	162.7306
2153	1548.03	1635.93	3.1840985	1141.535	14.07501	4886.097	163.1259	215.2192	162.3653
2156	1574.07	1638.37	1.4243591	1144.603	14.85208	4968.979	163.3573	216.2233	162.582
2167	6504.31	6803.52	1.0222967	270.79	4.884035	20025.5	183.8057	404.633	171.4908
2201	6537.93	6917.82	1.2106295	201.7442	5.772273	20109.67	181.5886	392.5793	173.916
2233	1597.67	1701.04	3.0923918	796.8485	8.285625	5044.281	163.0249	219.2407	162.4071
2213	1613.95	1684.76	1.5164416	836.8044	12.4688	5087.509	163.6883	217.6547	162.7295
2220	1620.46	1690.46	1.6694015	863.9312	10.64062	5112.047	163.3942	219.6683	162.6276
2239	1633.49	1705.92	1.9587206	874.0736	12.30704	5150.721	163.6958	219.232	162.821
2260	1650.58	1723.01	1.4650203	747.3622	12.07659	5197.106	163.9185	219.2801	162.8265
2285	1666.04	1743.36	1.5956451	688.5157	8.534645	5254.887	163.5154	221.4403	162.7828
2310	1694.53	1763.71	1.467797	687.2551	8.437114	5337.867	163.3692	219.2463	162.6107
2609	1932.19	2007.06	2.0052331	983.8416	8.898021	6076.06	162.7942	222.9502	162.4115
2629	1932.19	2023.34	1.8240443	232.1228	4.008499	6076.55	164.6385	226.257	163.8382
1770	1280.26	1324.21	2.0054683	938.3266	12.82792	4079.521	163.1413	207.1998	162.599
1782	1288.39	1333.97	3.1715562	727.8004	14.38951	4096.598	164.0027	206.8659	163.0287
1782	1289.21	1333.97	2.0463629	849.3187	15.11676	4097.356	163.7664	208.8204	162.816
1784	1294.91	1335.6	1.666154	713.8612	15.09307	4118.701	164.3818	207.8911	163.3835
1797	1306.3	1346.18	0.9670807	749.0828	13.18891	4151.633	163.8027	208.1157	162.9188
1809	5428.52	5599.98	0.9152849	467.1798	15.41243	16711.5	179.7112	352.2271	172.245
1803	5408.35	5579.8	0.9306086	220.0064	8.852445	16670.03	188.4489	371.0852	178.7326
1813	1310.37	1359.2	1.2974555	995.0014	11.41986	4171.188	162.9006	210.3812	162.4241
1815	1316.88	1360.83	1.0818884	354.0062	6.988595	4192.293	164.2321	209.5834	163.4929
1819	1317.7	1364.09	1.7979037	415.2706	7.873056	4198.496	163.8552	210.1598	163.3618
1821	1325.02	1365.71	1.2008604	467.3378	12.60013	4207.55	165.174	207.6075	163.792
1863	1325.02	1399.9	1.7675681	236.29	4.471678	4218.183	164.0786	210.8035	163.3703
1825	1326.65	1368.97	2.0627801	918.3703	15.6131	4209.743	163.6168	209.328	162.6728

1866	1328.28	1402.34	2.3840424	400.8095	8.436659	4219.179	164.4174	210.021	163.3196
1830	1332.35	1373.04	1.1463348	820.8889	16.77622	4230.594	164.3434	209.6303	163.2599
1879	1333.16	1412.92	1.5500702	407.4971	6.260835	4240.147	163.4931	209.6283	162.8522
1844	1336.41	1384.43	1.6617188	915.1027	9.688519	4249.779	162.7369	209.7319	162.2889
1885	1344.55	1417.8	2.7891933	783.4	10.676	4270.943	163.2692	210.7119	162.5855
1992	1454.43	1504.89	1.6612766	734.5969	14.41488	4603.966	164.2022	210.1674	163.1766
1997	1457.68	1508.96	2.129527	783.9767	11.77376	4616.989	163.5815	212.0011	162.8259
2006	1462.57	1516.29	1.6262183	832.9869	12.97046	4632.131	163.6931	212.3924	162.9076
2020	1479.66	1527.68	1.0698661	870.9946	21.62191	4674.096	164.7085	210.0416	163.2833
2033	1482.92	1538.26	1.6415401	730.5441	14.1605	4687.574	164.2356	213.2827	163.0865
2043	1482.1	1546.4	0.9649491	837.4563	7.725294	4702.658	162.8649	210.4398	162.0922
2071	1492.68	1569.19	1.8590094	856.3637	9.107319	4721.895	162.8881	214.4224	162.2911
2108	1507.33	1599.3	2.6799616	1003.505	13.3617	4762.149	163.1189	210.6718	162.3722
2107	1515.47	1598.49	2.0572857	858.7974	14.06953	4785.497	163.5485	210.5148	162.6159
2092	1518.73	1586.28	1.6562133	907.8123	11.39615	4811.894	163.1104	213.7112	162.6667
2092	1525.24	1586.28	1.0597939	847.7468	10.08789	4823.524	163.122	214.1188	162.4995
2108	1530.94	1599.3	1.3251565	614.1957	8.289967	4836.094	163.3035	213.2992	162.5268
2122	6319.41	6652.23	2.1729623	867.5644	10.42519	19473.78	170.2277	391.1829	167.3686
2134	6332.86	6692.58	1.6819028	474.409	6.410035	19533.82	171.0998	384.5205	168.3863
2142	1535.82	1626.97	2.2938494	808.6122	7.514885	4863.366	162.6353	215.2921	162.2706
2141	1539.07	1626.16	1.8092482	901.5844	9.734724	4864.615	162.9697	215.6993	162.3923
2167	1551.28	1647.32	2.3237056	824.3929	8.363653	4901.681	162.7928	213.8525	162.2453
2215	1551.28	1686.39	3.3258058	1364.646	8.857314	4909.904	162.1307	214.3286	161.8707
2162	1559.42	1643.25	1.9862846	965.6668	9.937658	4925.448	162.8134	213.9973	162.2412
2175	1568.37	1653.83	2.0775509	1026.332	16.0393	4945.634	163.5154	213.2721	162.5646
2196	1581.4	1670.93	2.2784381	1136.831	18.77134	4983.787	163.6249	213.8801	162.5981
2337	7011.95	7375.03	1.7182393	657.3505	10.13421	21573.31	172.0583	379.6636	168.4154
2345	6985.06	7401.93	2.4407586	909.282	9.000818	21522.41	168.4799	386.5442	166.4878
2342	1690.46	1789.75	2.158251	792.6502	7.685197	5331.771	162.8395	217.7354	162.3579
2385	7035.48	7536.4	1.4102505	219.5052	6.411606	21618.18	180.6477	384.0682	172.9944
2363	1701.04	1806.85	3.3510127	840.0067	12.0042	5354.812	163.7053	219.5166	162.7729
2379	1706.74	1819.87	2.3855709	701.4356	9.433337	5371.219	163.5053	219.1313	162.6232
2364	1707.55	1807.66	2.4490881	774.9467	10.35106	5370.396	163.4585	220.8234	162.5282
2385	1711.62	1824.75	2.6368922	927.795	11.2573	5388.01	163.2615	218.0264	162.5026
1827	1285.95	1370.6	1.7227422	370.0848	7.348462	4086.034	163.9693	208.087	162.9041
1949	1286.77	1469.89	2.2145741	885.1889	5.174272	4098.902	161.9018	208.1015	161.6865
1847	1316.07	1386.88	1.138895	400.039	7.236535	4182.541	163.7992	207.3807	162.9307
1864	1319.32	1400.71	1.1462839	264.7293	4.99886	4191.846	164.0641	209.9562	163.1577
2403	1718.95	1839.4	2.2269683	682.4788	5.477898	5417.985	162.5702	219.2997	162.1434
2367	1727.9	1810.1	1.6255293	733.5006	11.02491	5436.998	163.922	221.043	162.9169
2370	1718.95	1812.54	1.8018761	678.1112	6.693037	5425.41	162.9917	223.2186	162.5284

2405	1734.41	1841.03	2.6307757	790.8748	13.87567	5450.808	164.1569	220.6607	162.9276
2405	1731.15	1841.03	2.0973445	788.2369	6.099194	5466.799	162.4974	224.1971	162.2219
2393	1741.73	1831.26	1.7837324	891.6873	26.0986	5493.461	165.6606	220.6419	163.336
2393	1748.25	1831.26	1.6183899	697.4759	9.371411	5503.358	163.6713	220.5575	162.8469
2415	7233.83	7637.25	1.3775662	489.347	6.002381	22289.36	171.4909	416.3217	168.697
2417	1753.94	1850.8	2.1198674	989.9076	27.99402	5532.465	165.8213	216.8866	163.5838
2419	1766.96	1852.42	1.6776911	703.3221	12.68648	5552.843	164.1959	217.5506	163.0212
2385	1771.85	1824.75	0.9458545	698.3264	24.37396	5553.322	166.0248	218.2338	163.672
2400	1772.66	1836.96	0.9664937	800.6595	10.23233	5576.591	163.4836	219.4827	162.6966
2432	1780.8	1863	1.4128903	738.7912	10.02252	5599.592	163.4928	216.8721	162.6722
2503	1783.24	1920.79	2.4361993	779.4376	7.722348	5610.823	162.9942	221.1603	162.3887
2468	1789.75	1892.3	1.9270269	702.5702	8.132222	5632.783	163.3929	222.547	162.702
2457	1799.52	1883.35	2.2760606	1098.071	15.31567	5651.511	163.6186	221.58	162.6387
2497	1799.52	1915.91	2.0930779	595.7596	7.282666	5659.809	163.6722	226.8321	162.8246
2508	1797.89	1924.86	2.294495	630.3762	6.137695	5670.976	163.0461	227.371	162.6292
2513	1793.01	1928.93	3.5780117	893.1295	7.090867	5663.125	162.489	228.3948	162.2875
2657	1928.93	2046.13	2.3800143	746.1862	10.09736	6072.701	163.9516	226.1933	162.6395
2918	2180.42	2258.56	1.1615721	431.9664	5.526991	6832.962	164.0163	232.4297	163.2912
2924	2174.73	2263.44	1.9150672	723.4275	7.749573	6825.791	163.3992	235.4767	162.9828

Tab. 1: List of the important values of the best fit for each run number that is not noise or an empty data sheet.

References

- [1] <http://www.newlightsource.org/events/presentations/NLS%20photon%20science%20Priebe.pdf>
- [2] Glenn F. Knoll, Radiation Detection and Measurement. John Wiley & Sons, Inc., USA, 3rd Edition, 2000.
- [3] <http://www.upscale.utoronto.ca/GeneralInterest/DBailey/SubAtomic/Lectures/LectF05/Lect05.htm>

Appendix

MATLab code:

```
%% Gaussian fit and Chi2 test script with explanation

%% clear MATLAB
clear all
close all

%% to run all run numbers that are not noise or empty data sheets, include
% this section by taking out the percent signs in front of code in this
% section as well as the bottom of this page in front of "end" (line 262)
% beware! it will take a long time to run through all of the run numbers
%     load sheet.txt;
%     ASD = sheet(ZXC,2);
%     if ASD > 0
%         run_number=2195 + ZXC - 1;

%% input the run number that you are interested in (if doing all run numbers
% then put a percent sign in front of this run_number)
run_number=2208;

%% load the sheet with chosen-by-hand lower and upper channel numbers
load sheet.txt;

% the first row represents the lowest run number (value 2195)
a=run_number-2194;

% assign variables to lower and upper channels respectively
x_lo=sheet(a,4);
x_hi=sheet(a,6);

%% extracts specified spectra under "new"
file=sprintf('run%d.txt',run_number);
new=importdata(file);

% the total channel numbers for every spectra is 4096
maximum=4096;

%% selecting the value for the apex of the full energy peak
T=new(x_lo+maximum:x_hi+maximum);
[mx,indx]=max(T);
```

```

%% gaussian fit and Chi2 test

% Every lower channel number, "A", sweeps out the specified channel numbers
% "B". These sweeps range under "P", and "U". Make sure they range from 1
% to the same number.
for P=1:30
    for U=1:30

        % the number of channels swept by P and U should be the same value
        % as the value being subtracted in A so the analysis won't overlap
        % into the unusable data
        A=indx+x_lo+P-30;
        B=x_hi+U+00;

        % takes specified range from the spectra
        K=new(A:B);

        % add maximum to extract the full-energy peak (blue on 2D plots)
        L=new(A+maximum:B+maximum);

        % transverse matrices for Gaussian fit
        X=K';
        Y=L';

        % gaussian fit specified under "cf_"
        gaussfit= fitttype('gauss1');
        cf_=fit(X,Y,gaussfit);

        % add decimal places for accuracy
        format long

        % coefficient values for Gaussian fit
        coeff = coeffvalues(cf_);
        a1=coeff(1,1);
        b1=coeff(1,2);
        c1=coeff(1,3);

        % fit with coefficient values
        y=a1*exp(-(X-b1)/c1).^2);
        for j=1:length(Y)
            if(Y(j)<=1)
                Y(j)=1;
            end
        end

        % coefficient values being saved for every run
        coefficients=sprintf('%d_coeffval.txt',run_number);
        dlmwrite(coefficients,coeff, '-append', 'newline', 'pc', 'precision',

20);

        % Chi2 test; DOF is degrees of freedom
        Chisquare = sum((Y-y).^2./Y);

```

```

        DOF = length(Y)+2;
        Z = Chisquare/DOF;

        % Chi2 values being saved for every run; F = [A B Z] is saved, where
        % "A" and "B" are the lower and higher channel number, while Z is
        % the corresponding Chi2 value.
        filesaved=sprintf('%d.txt',run_number);
        F=[A B Z]
        dlmwrite(filesaved, F, '-append', 'newline', 'pc', 'precision', 20);
    end
end

%% Chi2 3D contour

% open Chi2 values with respect to lower and upper channel numbers
new2=importdata(filesaved);

% make grid range from varying values of lower and upper channel numbers
rangeX=(min(new2(:,1))):(max(new2(:,1)));
rangeY=(min(new2(:,2))):(max(new2(:,2)));
[xi,yi] = meshgrid(rangeX,rangeY);

% overlay Chi2 values with grid
zi=griddata(new2(:,1),new2(:,2),new2(:,3),xi,yi);

% make figure
figure;
hold on;
surf(xi,yi,zi);
ZZ=surf(xi,yi,zi);
colorbar;
xlabel('LoBndChnl#');
ylabel('HiBndChnl#');
zlabel('Chi2Val');

%%%%%%%%%%%%%%%%%%%%%%%%%%%%%%%%%%%%%%%%%%%%%%%%%%%%%%%%%%%%%%%%%%%%%%%%%%%%%%
%%% In this is optional to display a "wall" showing the useful low channel
limit
%%% making useful channel upper limit by highlighting the apex of the full
%%% energy peak. T is the full energy peak
T=new(x_lo+maximum:x_hi+maximum);

%%% assign apex channel number to "indx" and make wall so you can see on
%%% Chi2 3D contour
[mx,indx]=max(T);
UsflChanLim=indx+x_lo;
n=size(xi);
n1=n(1,1);
m=repmat(UsflChanLim,n1,n1);

%%% put limit on contour
%plot3(m,yi,zi);

hold off;

```

```

%%% extract up to useful channel upper limit
Q1=(xi(1,:));
[ROW,COL] = find(Q1==Usf1ChanLim);
Q2=(zi(:,1:COL));
%%%%%%%%%%%%%%%%%%%%%%%%%%%%%%%%%%%%%%%%%%%%%%%%%%%%%%%%%%%%%%%%%%%%%%%%

% find minimum Chi2 value
Q3=min(Q2);
MinChi2Val=min(Q3);
[ROW2,COL2]= find(zi==MinChi2Val);

% find lower and higher channels with respect to minimum Chi2 value
XloChan=xi(1,COL2);
XhiChan=yi(ROW2,1);

% find corresponding values to the lower and higher channels with respect
% to the minimum Chi2 value
XloVal=new(XloChan,1);
XhiVal=new(XhiChan,1);

% save Chi2 3D contour with useful channel upper limit
myfig = sprintf('%d_3Dchi2.fig',run_number);
saveas(gca,myfig,'fig');

%% Plot the Gaussian fit with respect to the minimum Chi2 value over the
spectrum

% make variables to represent whole spectrum
Xx=new(:,1);
Yy=new(:,2);

% make variables ranging from the lower to higher channel limits specified
% from the minimum Chi2 value
XXx=new(XloChan:XhiChan,1);
YYy=new(XloChan:XhiChan,2);

% make figure
figure;
hold on

% plot the two; they will overlap perfectly
plot(Xx,Yy);
plot(XXx,YYy);

% gaussian fit only over the specified channels from minimum Chi2 value
cf_1 = fit(XXx,YYy,gaussfit);

% plot the gaussian over spectrum
plot(cf_1);
hold off

```

```

% save full spectrum with gaussian fit
myfig1 = sprintf('%d_cftool.fig',run_number);
saveas(gca,myfig1,'fig');

% coefficient 95% confident bounds (you can change confidence bounds 0 - 1)
CB = confint(cf_1,.95);

% creating variables for (-/+) confidence bounds
a2 = CB(1,1);
a3 = CB(2,1);
b2 = CB(1,2);
b3 = CB(2,2);
c2 = CB(1,3);
c3 = CB(2,3);

a4 = a2 - a1;
a5 = a3 - a1;
b4 = b2 - b1;
b5 = b3 - b1;
c4 = c2 - c1;
c5 = c3 - c1;

%% Display

% respectively: the gaussian fit, lower and higher channels and then values
% corresponding to the minimum Chi2 value, and minimum Chi2 value
cf_1
XloChan=xi(1,COL2)
XhiChan=yi(ROW2,1)
XloVal=new(XloChan,1)
XhiVal=new(XhiChan,1)
MinChi2Val=min(Q3)

%% saving values

% BestFit file lists optimum values corresponding to the minimum Chi2 value
% listed as: run_number XloChan XhiChan XloVal XhiVal MinChi2Val
BestFitVal=[run_number XloChan XhiChan XloVal XhiVal MinChi2Val];

BestFit=sprintf('%d_BestFit.txt',run_number);
dlmwrite(BestFit,BestFitVal, '-append', 'newline', 'pc', 'precision', 20);

AllBestFit=sprintf('AllBestFit.txt');
dlmwrite(AllBestFit,BestFitVal, '-append', 'newline', 'pc', 'precision', 20);

% BestCoeff file lists the coefficients of the best gaussian fit
% listed as: run_number a1 (-/+) b1 (-/+) c1 (-/+) or A = a1, mu = b1, sigma
= c1/(sqrt(2))
BestCoeffVal=[run_number a1 a4 a5 b1 b4 b5 c1 c4 c5];
BestCoeff=sprintf('%d_BestCoeff.txt',run_number);
dlmwrite(BestCoeff,BestCoeffVal, '-append', 'newline', 'pc', 'precision',
20);

AllBestCoeff=sprintf('BestCoeff.txt');

```

```
dlmwrite(AllBestCoeff,BestCoeffVal, '-append', 'newline', 'pc', 'precision',  
20);  
%     end
```

MATLab code for data analysis.

Appendix 3: Analysis of ^{235}U photofission near the barrier (preliminary). R. Espinoza (final results to be published in thesis)

Low energy fission can be described in terms of a highly deformed transition state nucleus with a few excitation levels. Since most of the excitation energy goes into deforming the nucleus to a saddle-point, the nucleus can be seen as thermodynamically "cold" at this point. From here fission can only occur through a few channels which are directly linked to the nucleus's quantum numbers J, K, and M. Fission fragment angular distributions offer a way to access this information since it is directly linked by the same quantum numbers (J, K, and M) as the nucleus's fissioning channels.

The fission fragment angular distribution theory can be modeled by characterizing the axially symmetric transition states at the saddle of the fissioning nucleus with the behavior of an axially symmetric top. It is assumed that the fission fragments separate along the symmetric axis at the scission point.

A symmetric top is defined as a rigid body with two of its moments of inertia equal to each other (assuming three total moments of inertia) as seen in Figure 1. The space fixed axis, Z, is taken as the incident beam's direction. J is the total angular momentum and M is J's projection on Z. The K vector is the component of J that is along the nuclear symmetry axis. The rotational angular momentum, R, is the vector that is perpendicular to the nuclear symmetry axis. Both J and M are constants of motion due to conservation rules. Although K isn't constrained to be fixed it is assumed that when the nuclei reaches the transition state K will remain fixed and therefore a 'good' quantum number. Up until this point, however, K isn't constrained to be any particular value. [Put stuff about K being good only later on in the process].

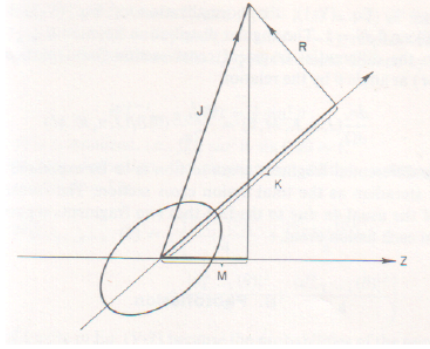


FIG. 1. A diagram for the angular momentum for a deformed nucleus.

The quantum mechanical wave equation for a symmetric top can be written as,

$$\frac{\hbar^2}{2J_{\perp}} \left[\frac{1}{\sin(\Theta)} \frac{\partial}{\partial \Theta} \left(\sin(\Theta) \frac{\partial \Psi}{\partial \Theta} \right) + \frac{(\cos(\Theta) \frac{\partial}{\partial X} - \frac{\partial}{\partial \Phi})^2 \Psi}{\sin^2 \Theta} \right] + \frac{\hbar^2}{2J_{\parallel}} \frac{\partial^2 \Psi}{\partial X^2} + E\Psi = 0. \quad (1)$$

J_{\perp} and J_{\parallel} are the moments of inertia perpendicular and parallel to the symmetry axis respectively. Φ, X , and Θ are the Euler angles of the top. This wave equation has already been solved (cite) using separation of variables and its solution is given as,

$$\Psi = \left(\frac{2J+1}{8\pi^2} \right) e^{iM\Phi} e^{iKX} d_{K,M}^J(\Theta) \quad (2)$$

The $d_{K,M}^J(\Theta)$ function is the differential wave function which is defined as (cite),

$$|d_{M,K}^J| = [(J+M)!(J-M)!(J+K)!(J-K)!]^{1/2} \sum_X \frac{(-1)^X [\sin(\Theta/2)]^{K_M+2X}}{(J-K-X)!(J+M-X)!(X+K-M)!X!}. \quad (3)$$

Given some nuclear state defined by its quantum numbers J, K, M and by the space $(\Phi, \Phi+d\Phi), (X, X+dX), (\Theta, \Theta+d\Theta)$, the probability can be written as,

$$|\Psi^2| \sin(\Theta) d\Theta d\Phi dX = W_{K,M}^J(\Theta) \sin(\Theta) d\Phi dX d\Theta \quad (5)$$

where $W_{K,M}^J(\Theta)$ is the fission fragment angular probability. Integration over the cyclic coordinates (Φ and X) then yields,

$$W_{K,M}^J(\Theta) = \frac{2J+1}{2} |d_{M,K}^J|^2 \quad (6)$$

with the condition that,

$$\int_0^\pi W_{K,M}^J(\Theta) \sin(\Theta) d\Theta = 1. \quad (7)$$

If it is assumed that there is only electric dipole absorption, it can be seen that there are variety of possible states for which an atom can decay depending on its spin. To construct a full expression for the angular distribution of fission fragments it is necessary to sum up these possible states as follows,

$$W_{\gamma,f}(\Theta) = \sum_J \sum_M \sum_K X_J * P_K * W_{M,K}^J(\Theta) \quad (8)$$

Since the target under study in this paper is ^{235}U and has a spin of $J=9/2$ (target details in Table I), the nucleus can decay through $K=\frac{9}{2}, \frac{7}{2}, \frac{5}{2}, \frac{3}{2}$, or $\frac{1}{2}$ with an inherent probability (P_K) associated with each possible decay channel. Including this into the definition of the full angular distribution of fission fragments we have the following:

$$W_{\gamma,f}^{235\text{U}}(\Theta) = \sum_K W_K(\Theta) \quad (9)$$

$W_K(\Theta) :$

$$W_{1/2}(\Theta) = P_{1/2} * \left[\left(X_{5/2} * \sum_M W_{\pm M, \pm 1/2}^{5/2} \right) + \left(X_{7/2} * \sum_M W_{\pm M, \pm 1/2}^{7/2} \right) + \left(X_{9/2} * \sum_M W_{\pm M, \pm 1/2}^{9/2} \right) \right] \quad (10)$$

$$W_{3/2}(\Theta) = P_{3/2} * \left[\left(X_{5/2} * \sum_M W_{\pm M, \pm 3/2}^{5/2} \right) + \left(X_{7/2} * \sum_M W_{\pm M, \pm 3/2}^{7/2} \right) + \left(X_{9/2} * \sum_M W_{\pm M, \pm 3/2}^{9/2} \right) \right] \quad (11)$$

$$W_{5/2}(\Theta) = P_{5/2} * \left[\left(X_{5/2} * \sum_M W_{\pm M, \pm 5/2}^{5/2} \right) + \left(X_{7/2} * \sum_M W_{\pm M, \pm 5/2}^{7/2} \right) + \left(X_{9/2} * \sum_M W_{\pm M, \pm 5/2}^{9/2} \right) \right] \quad (12)$$

$$W_{7/2}(\Theta) = P_{7/2} * \left[\left(X_{5/2} * \sum_M W_{\pm M, \pm 7/2}^{5/2} \right) + \left(X_{7/2} * \sum_M W_{\pm M, \pm 7/2}^{7/2} \right) + \left(X_{9/2} * \sum_M W_{\pm M, \pm 7/2}^{9/2} \right) \right] \quad (13)$$

$$W_{9/2}(\Theta) = P_{9/2} * \left[\left(X_{5/2} * \sum_M W_{\pm M, \pm 9/2}^{5/2} \right) + \left(X_{7/2} * \sum_M W_{\pm M, \pm 9/2}^{7/2} \right) + \left(X_{9/2} * \sum_M W_{\pm M, \pm 9/2}^{9/2} \right) \right]. \quad (14)$$

The X_J terms are the width ratios which don't vary in value within the different K states. X_J is defined as,

$$X_J = (\Gamma_f^J / \Gamma_T^J) = \frac{T_{\lambda f}(J, -, K, E)}{T_{\lambda \gamma}(J, -, E) + T_{\lambda f}(J, -, K, E) + T_{\lambda n}(J, -, K, E)} \quad (15)$$

where Γ_i^J are fission barrier widths and $T_{\lambda i}$ are the fission barrier transmission coefficients.

Much of experimental data on fission fragment angular distributions has been gathered using a Bremsstrahlung radiation photon source that bombards the target with a large spread of photon energies. Fission fragment angular distributions have been studied with such sources and generally agree with the current theory, but this method lacks the ability to probe into any fission barrier structure. Many techniques have been developed to try to make up for this spread of energy, but it still has too broad of a spectrum to study the fission barrier with much precision. With the development of nearly mono-energetic photon sources it is now possible to take data without the need for much compensation for beam spread. The use of the narrow beam provided by HI γ S allows a chance for a deeper evaluation of what is known about the fission barriers of fissile nuclei. It is customary to assume that only 1 decay channel contributes, however, in order to explore the photo-fission process in greater detail the effects of the other channels were included and varied according to a Gaussian distribution,

$$P_K = \frac{1}{\sigma \sqrt{2\pi}} \exp \left[-\frac{(K - \mu)^2}{2\sigma^2} \right] \quad (16)$$

where μ is the mean and σ is the standard deviation. For the purposes of analyzing the experimental data, the mean was set to $\mu = \frac{1}{2}$. By having a Gaussian distribution we can easily vary the effect that the other K states have by varying σ .

II. EXPERIMENTAL PROCEDURE

Photofission of a ^{235}U target was studied for this work. The details of the target are in Table I. The High Intensity γ -ray Source (HI γ S) provided a nearly mono-energetic γ -ray source that can be tuned across a wide range of energies and switched between linear and circular polarizations. HI γ S is a Free-Electron laser (FEL) based Compton backscattering source that works by mixing a two-bunch electron beam in a storage beam with the high powered FEL. With a wavelength of approximately 540 nm, the FEL beam energies were chosen to produce 179 ns pulsed γ -ray beams that ranged through 5.6-7.3 MeV (This needs to be double checked!) with a FWHM of about 3%. A set of precision Cu attenuators and a large NaI detector were used to measure the absolute intensity. The intensity ranged from 3×10^6 to 7×10^6 γ/s .

Target	Dimensions	Mass (g)	Enrichment (%)	Main Impurity
^{235}U	5mm x 10mm	4.620	93.7	^{238}U (6.3%)

TABLE I. Details of the target used for photofission



FIG. 2. The detector array in which the target was placed in the center.

Perpendicular Detectors (θ, ϕ)	$(55^\circ, 0^\circ)$	$(90^\circ, 0^\circ)$	$(107^\circ, 0^\circ)$	$(125^\circ, 0^\circ)$	$(142^\circ, 0^\circ)$
Parallel Detectors (θ, ϕ)	$(72^\circ, 90^\circ)$	$(107^\circ, 90^\circ)$	$(125^\circ, 90^\circ)$	$(142^\circ, 90^\circ)$	

TABLE II. The positions of the acceptable detectors that were used in the analysis of photofission angular fission fragment distribution.

Information about the neutrons produced from photofission was detected using a collection of 18 detectors as seen in Figure 2. Twelve of the detectors were arranged at $\Theta = 55^\circ, 90^\circ$ and 125° with the azimuthal angle, ϕ , set at $\phi = 0^\circ$, $\phi = 90^\circ$, and 180° for each value of Θ . The other six detectors were placed at $\Theta = 72^\circ, 107^\circ$ and 142° with $\phi = 0^\circ$ and 90° . The ^{235}U target was placed in the center of the detector array which give an approximate flight path to the detectors of 57 cm. The active volume, 12.7cm diameter and 5.1cm thick (Check this!), of each detector contained BC-501A liquid scintillator.

The fission neutrons were determined using a time of flight method. Cut offs were put in place to isolate the gamma rays produced from the fission neutrons from those produced from other processes. The neutrons produced from non-fission processes typically are concentrated in a narrow energy band that is generally low in energy. Given the nature of the fission process, the neutrons produced by the fission process have a broad energy spectrum that extends out to a fairly high energy. Given this difference, it is simple to set a threshold that cuts out all of the concentrated low energy gamma rays that represent non-fission neutrons. In the case of this experiment the threshold was set to 1.5 MeV. More details of the data reduction and analysis that was used in this experiment can be found in (Muellers paper).

III. ANALYSIS

The standard method of analyzing fission fragment angular distributions is to fit data using the general theoretical model given by (cite):

$$W(\theta) = a + b * \sin^2(\theta) + c * \sin^2(2\theta) \quad (17)$$

where a represents the isotropic portion, b is the level of anisotropy, and c is the quadrapole component. Given the target under study in this paper there is a negligible quadrapole contribution so it is being left out of the analysis.

According to Huizenga, for odd-mass targets with a large spin, the fission fragment angular distribution can be calculated assuming that $T_{\lambda f}(J, -, K, E)$ is much greater than $T_{\lambda \gamma}(J, -, E)$ and that $T_{\lambda f}(J, -, K, E)$ values are independent of J . In other words, the fission transmission coefficients of the rotational members of a particular band are equal (The X_J terms are all equal). This is why the fission fragment theory can be generalized down to Eq. 17.

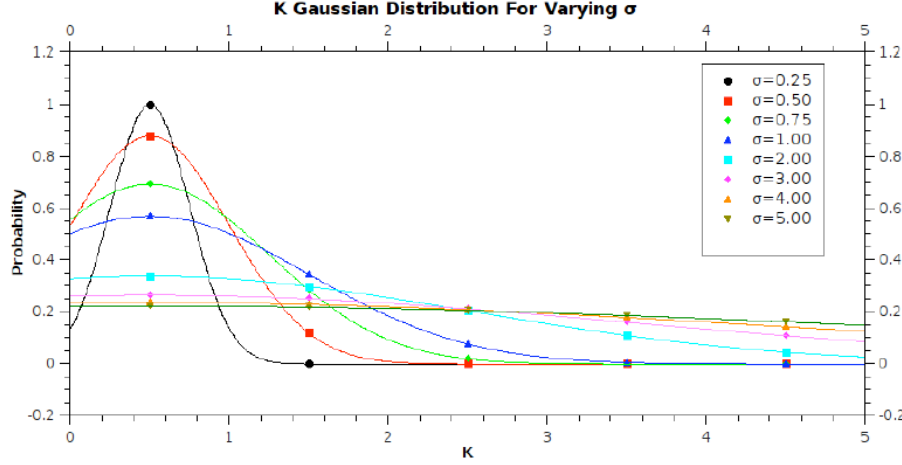


FIG. 3. K-state probability distributions for varying σ .

Instead of making this reduction, the X_J values were left as free parameters in order to study the affects of these assumptions and to explore if any trends become apparent given the narrower photon energy spread possible with the HI- γ S photon source.

The experimental data was fit using the theoretical angular distribution, $W_{\gamma,f}^{235U}(\Theta)$ (Eq.10-14), where the fit parameters were the width ratios (X_J). Since the X_J terms are inherently energy dependent they should reveal any anisotropy or structure due to variations in photon energy. Equations 10-14 are evaluated with to have the following values:

$$W_{K=1/2}(\Theta) = P_{1/2} * \left[\frac{3}{28} + \frac{3}{112}\sin^2(\Theta) \right] X_{5/2} + \left[\frac{31}{126} - \frac{5}{42}\sin^2(\Theta) \right] X_{7/2} + \left[\frac{5}{36} + \frac{5}{48}\sin^2(\Theta) \right] X_{9/2} \quad (18)$$

$$W_{K=3/2}(\Theta) = P_{3/2} \left[\frac{27}{224} + \frac{3}{448}\sin^2(\Theta) \right] X_{5/2} + \left[\frac{3}{14} - \frac{1}{14}\sin^2(\Theta) \right] X_{7/2} + \left[\frac{5}{32} + \frac{5}{64}\sin^2(\Theta) \right] X_{9/2} \quad (19)$$

$$W_{K=5/2}(\Theta) = P_{5/2} \left[\frac{33}{224} - \frac{15}{448}\sin^2(\Theta) \right] X_{5/2} + \left[\frac{19}{126} + \frac{1}{42}\sin^2(\Theta) \right] X_{7/2} + \left[\frac{55}{228} + \frac{5}{192}\sin^2(\Theta) \right] X_{9/2} \quad (20)$$

$$W_{K=7/2}(\Theta) = P_{7/2} \left[\frac{1}{18} + \frac{1}{6}\sin^2(\Theta) \right] X_{7/2} + \left[\frac{35}{144} - \frac{5}{96}\sin^2(\Theta) \right] X_{9/2} \quad (21)$$

$$W_{K=9/2}(\Theta) = P_{9/2} \left[\frac{5}{16} - \frac{5}{32}\sin^2(\Theta) \right] X_{9/2}. \quad (22)$$

The probabilities, P_K , that were used in this analysis can be seen in Table II or Figure 3. They were calculated using Eq. 16 where σ was varied to increase the role that the other K-states had. A least squares fitting algorithm was used to fit the experimental data to the theoretical fission fragment angular distribution. Although there was a total of eighteen detectors that gathered data, only a few were acceptable to use in analysis since some of the detectors proved to be problematic after the experiment was completed. Table III shows which of the detectors were used.

The range of K-state distributions was chosen after analysis of the behavior of the fit for a range of distributions that start from having K=1/2 solely dominating and out to a point where the states all shared an appreciable weight. Figure 14 shows this analysis out to $\sigma = 5$ where it becomes apparent that the error increases as more weight is placed on the other K-states. From this result it was then decided to limit our analysis to distributions between having an exclusive K=1/2 dominance out to a Gaussian distribution with $\sigma = 1$.

P_K	Only K=1/2	$\sigma = 0.25$	$\sigma = 0.50$	$\sigma = 0.75$	$\sigma = 1.0$
$P_{1/2} = 1.0$		0.99967	0.88054	0.69444	0.57035
$P_{3/2} = 0.0$		0.00033535	0.11917	0.28549	0.34594
$P_{5/2} = 0.0$		1.26600×10^{-14}	0.00029539	0.019837	0.077188
$P_{7/2} = 0.0$		5.3784×10^{-32}	1.3411×10^{-8}	0.00023296	0.0063360
$P_{9/2} = 0.0$		2.5714×10^{-56}	1.1151×10^{-14}	4.6238×10^{-7}	0.00019133

TABLE III. K-state probability distributions for varying σ .

IV. RESULTS

Figures 4-5 show samples of the detector data that was fit using the previously mentioned prescription. Average χ^2 values for the perpendicular detector data was about 18 whereas for the parallel detectors it was 251. While these are fairly high values of χ^2 it was mainly caused by the lack of usable data. From the 18 original detectors only 5 were used in the perpendicular detector analysis and 4 for the parallel. The fitting algorithm used to fit the data had trouble finding the correct minimum for any given data set, so the initial conditions that were used affected the outcome of the fit quality greatly. Given all this, however, it was seen that the relative values of the fitting parameters (X_J) didn't deviate much under various conditions used while trying to maximize the fitting quality. This allowed the overall features seen in the results to remain unclouded by the errors.

Figures 6-10 show the results of the fits for the various K-state distributions. A complete table of all the X_J results can be seen in the appendix. Only the analyzed data for the perpendicular detectors are shown in the figures since the results of the parallel detectors showed no significant change in the results, but include the increased fit quality as previously mentioned. An analysis of the differences between the detector results are shown in Figures 11. Although there is no statistical difference between the detectors, it seems as though there is a general trend of separation between the parallel and perpendicular detectors. Figure 12 shows this more clearly in that the perpendicular detectors have a distinct trend of having a smaller values when compared to the parallel data. The errors involved in the parallel data were larger, as previously discussed, and mask any conclusive statistical separation. It is likely that is the errors were reduced some measurable anisotropy would be present.

What is clear from the data is that the $X_{9/2}$ term dominates over the other X_J terms. $X_{5/2}$ is consistently negligible in terms of its contribution whereas $X_{7/2}$ is seen to contribute only a very small fraction to the fit. Figure 13 illustrates the role that each X_J term has on the overall fit. From the figure it is apparent that term including $X_{9/2}$ seems to fit the form of $W(\theta)$ closely and with $X_{5/2}$ term looking somewhat similar. The $X_{5/2}$ term has the wrong slope compared to $W(\theta)$ so it isn't surprising that the results point to the $X_{5/2}$ being of negligible influence.

The X_J values were seen to have a negligible change over the the span of the photon energies that were used. For each change in K-state distribution the values remained relatively unaffected. Figure 14 shows closer look at the effect that spreading the influences that each of the K-states had on the overall X_J values. As the this distribution increased it was apparent the the errors increased as well, but there seemed to be a general trend forming. Distributions past $\sigma = 1$ showed that the effect of $X_J = 9/2$ increased while the other two widths started decreasing in contribution.

The results of this analysis shows that photo-fission in ^{235}U has a clear spin dependence. From the fission fragment distribution theory it isn't surprising that the $X_{9/2}$ term dominated over the other terms. Since fission involves a nucleus breaking apart due in instability, it makes sense from a classical perspective, that the term with the highest spin would contribute the most to fission. The analysis agrees by showing the $J = 9/2$ fission channel with the largest contribution and with the $J = 7/2$ coming in second, but only weakly contributing. The $J = 5/2$ channel's contribution to fission is seen to be as negligible. It's interesting to note that results of this analysis show that the contribution of the X_J remain relatively the same across the entire energy spectrum that was used. This shows that the relative energy dependence of X_J is weak across the few MeV where data was gathered.

The largest source for the error encountered in this analysis stemmed from uncertainty in the fission neutron measurements. These uncertainties propagated throughout the analysis and ultimately disguised some of the results. This is, however, to be expected on some level due to the photon beam's comparative size to the fission barrier energy levels. In Figures 6-10 there are fairly large error bars across most of the spectrum, however, these uncertainties aren't large enough to discredit the distinct separation between the X_J values. These results are clear and without any special modification of the data, as would be done if the data was gathered using a different photon source (i.e. Bremsstrahlung).

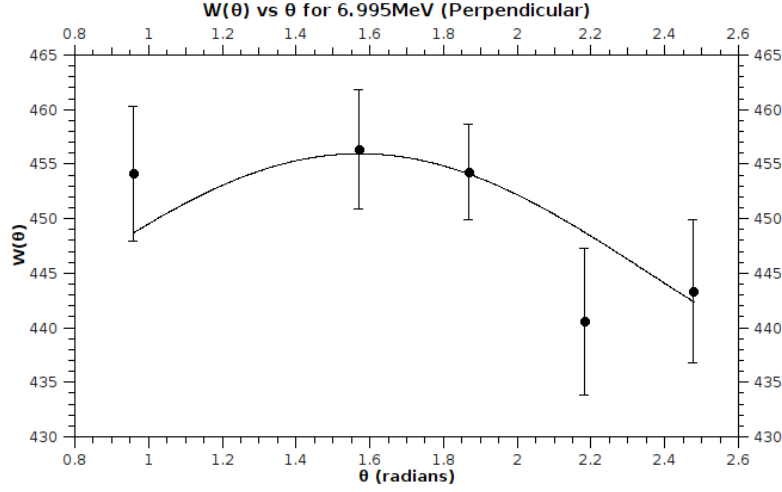


FIG. 4. A sample of the perpendicular detector data that was fit with the prescribed method given in this paper.

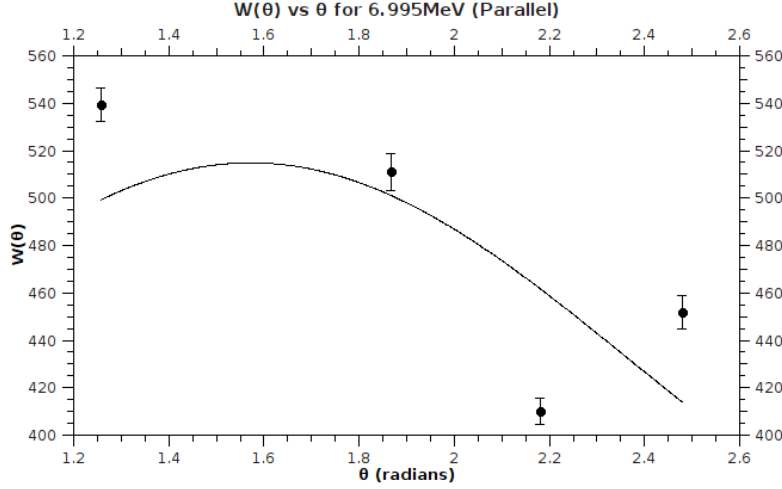


FIG. 5. A sample of the parallel detector data that was fit with the prescribed method given in this paper. The results of the parallel detectors were similar to that of the perpendicular detector data, but tended to have a higher degree of uncertainty due to the lack of usable detectors.

The directness of this technique to probe and analyze fission barriers suggest that it would be possible to explore the lower energy regions of the fission barrier in search of structure that isn't accurately modeled with the current smooth fission fragment theory. With the current analysis it's seen that at lower energies the error increases, which can be associated with the board beam triggering more of the competing non-fission processes and detracting from the total fission neutron count. In order to study this region more effectively it will be necessary to either increase the amount of time data is gathered to compensate for the overall lower fission probability or to use a narrower beam that can access the small gaps between the energy levels. The low statistics in this region limited the exploration of this region for this paper.

The current understanding is that the fissioning channels at the fission barrier have the same structure as those of the non-fissioning decay channels, but are compressed as illustrated in Figure 15(cite). If this is true we'd expect that

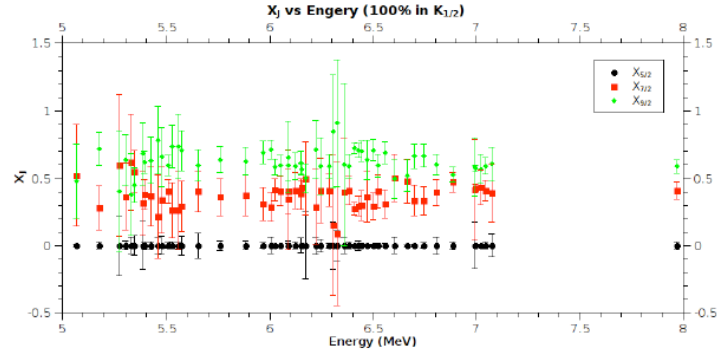


FIG. 6. Normalized X_J values for the case where $K=1/2$ is the only contributor to the angular fission fragment distribution. This graph is only for the perpendicular detectors.

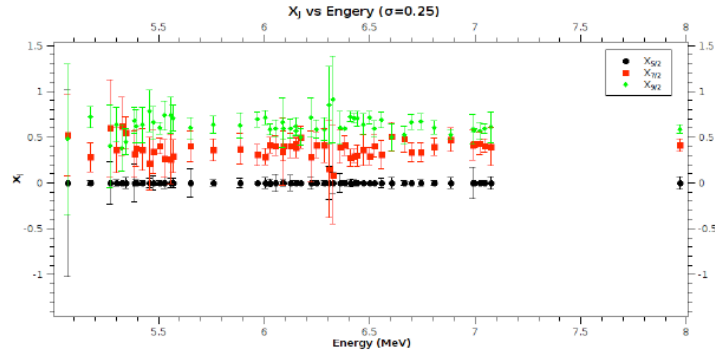


FIG. 7. Normalized X_J values for the case of a K-state distribution with $\sigma = 0.25$. This graph is only for the perpendicular detectors.

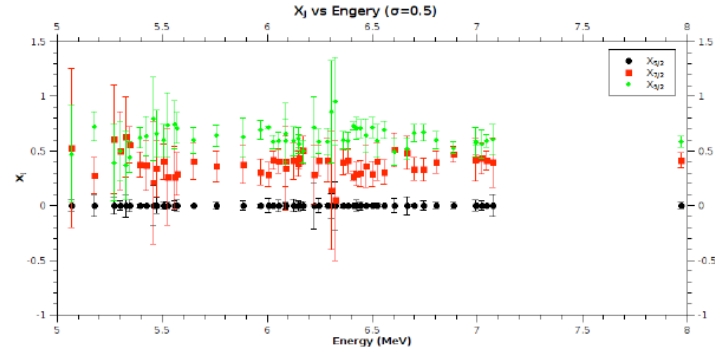


FIG. 8. Normalized X_J values for the case of a K-state distribution with $\sigma = 0.50$. This graph is only for the perpendicular detectors.

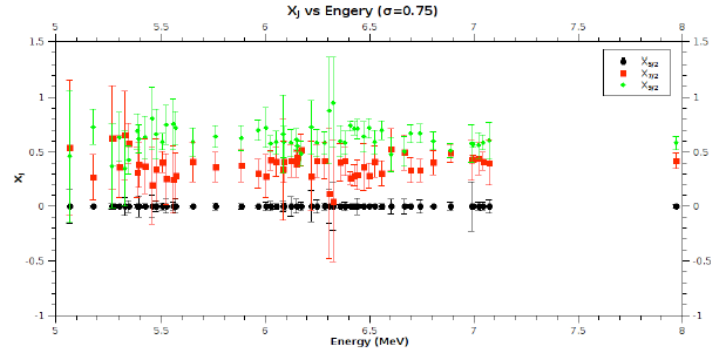


FIG. 9. Normalized X_J values for the case of a K-state distribution with $\sigma = 0.75$. This graph is only for the perpendicular detectors.

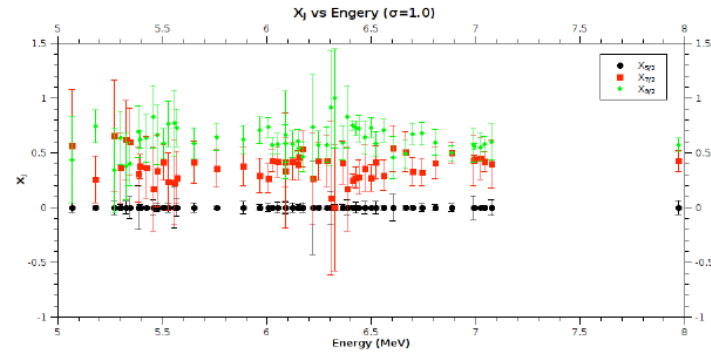


FIG. 10. Normalized X_J values for the case of a K-state distribution with $\sigma = 1.0$. This graph is only for the perpendicular detectors.

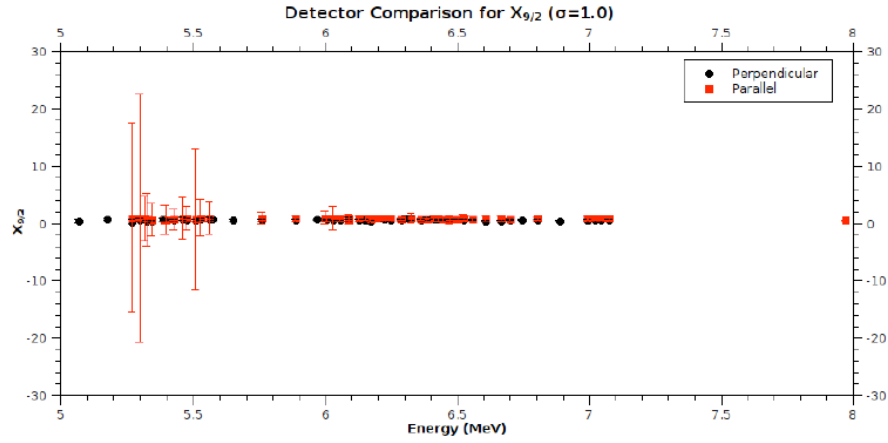


FIG. 11. A comparison of perpendicular and parallel detector results for $X_{9/2}$ and $\sigma = 1$. Similar results are seen for all cases of X_J and K-state distributions.

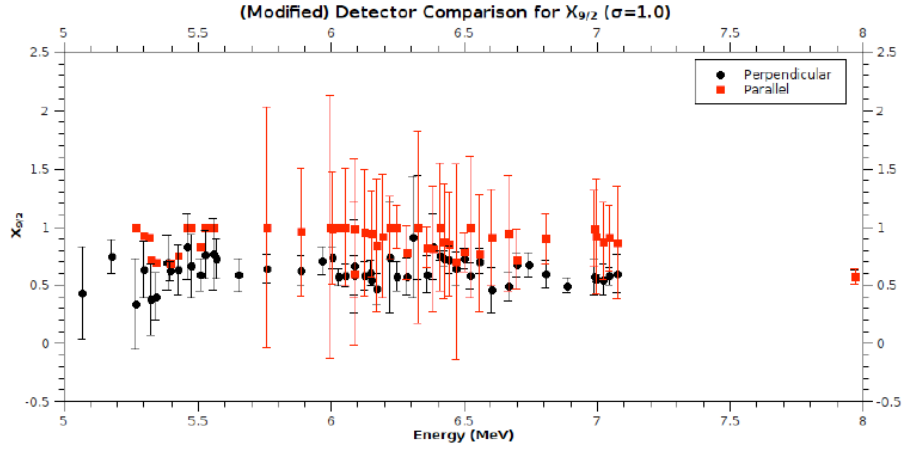


FIG. 12. The same data in Figure 13 with the error bars for some of the data removed in order to have a closer look at how the detectors compare. The points at the following energies had their error bars removed: 5.27, 5.301, 5.318, 5.326, 5.344, 5.393, 5.424, 5.458, 5.474, 5.526, 5.557, and 6.026 MeV

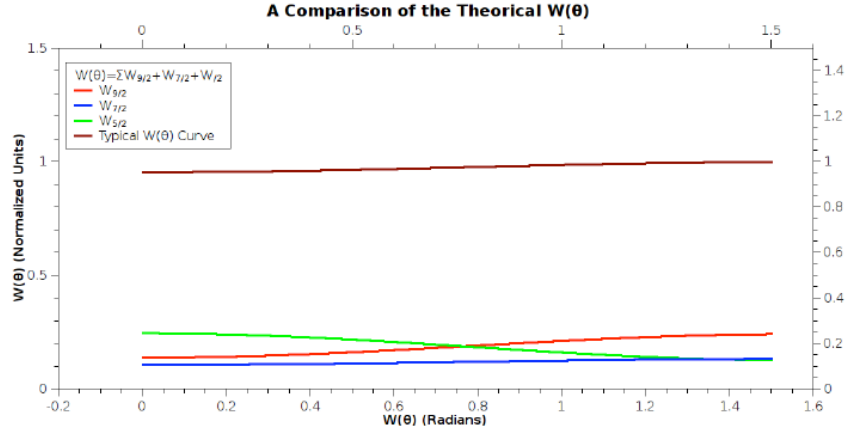


FIG. 13. A comparison of how the fit parameters work together to form the complete $W(\theta)$ distribution. The curve the represents the total $W(\theta)$ is a general case. All of the data that was analyzed had a similar shape for $W(\theta)$.

when the photon energy reaches levels of the $7/2^-$ ground state, just above the fission barrier, that the $X_J = 7/2$ term will dominate.

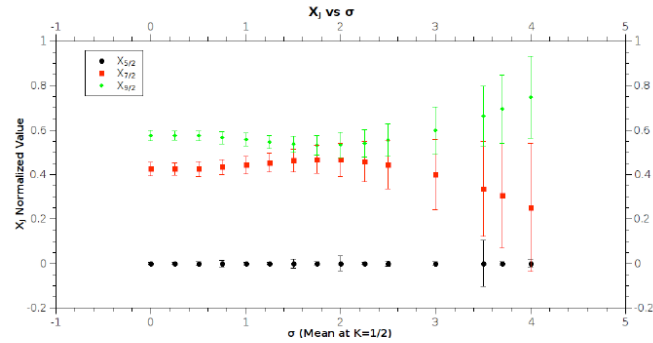


FIG. 14. An analysis of the effects of various K-state Gaussian distributions as σ is adjusted to increase the role the higher K-states have in the fit. As σ is increased, so that the distribution is more even across the different K-states, the error increases. The values up to $\sigma = 1$ were used to sample the effects that a K-state distribution has on the angular fission fragment distribution.